Available online at www.sciencedirect.com
SCIENCE DIRECT®
Earth and Planetary Science Letters 244 (2006) 186–200
EPSL
www.elsevier.com/locate/epsl

Evolution of fracture permeability through fluid–rock reaction under hydrothermal conditions

Hideaki Yasuhara [a,*], Amir Polak [b], Yasuhiro Mitani [c], Abraham S. Grader [d], Phillip M. Halleck [d], Derek Elsworth [d]

[a] *Department of Civil and Environmental Engineering, Ehime University, 3 Bunkyo-cho, Matsuyama, Ehime, 890-8577, Japan*
[b] *Civil and Environmental Engineering, Technion, Israel Institute of Technology, Haifa 32000, Israel*
[c] *Institute of Environmental Systems, Dept. of Civil Engineering, Faculty of Engineering, Kyushu University, 6-10-1, Hakozaki, Higashi-ku, Fukuoka, 812-8581, Japan*
[d] *Energy Institute and Department of Energy and Geo-Environmental Engineering, Pennsylvania State University, 403 Academic Activities Building, University Park, PA 16802, USA*

Received 20 July 2005; received in revised form 18 January 2006; accepted 22 January 2006
Available online 15 March 2006
Editor: R.D. van der Hilst

Abstract

We report flow-through experiments on a natural fracture in novaculite under moderate effective stresses (~1.4 MPa) and temperatures (20–120 °C) to examine the effect on flow and transport characteristics. The efflux of fluid and dissolved minerals were measured throughout the 3150-h experiment. After the experiment the fracture was imaged by X-ray CT, impregnated with Wood's metal, and a cast recovered of the Wood's metal-filled fracture. These measurements constrain the evolution of fracture structure, and the change in permeability that resulted from stress- and temperature-dependent dissolution at both propping asperities and fracture void surfaces. During the first 1500 h, the aperture of one fracture decreased from 18.5 to 7.5 μm, when it was loaded with constant effective stress of 1.4 MPa, at room temperature, and a flow rate decreasing with time from 1 to 0.0625 mL/min. This reduction is attributed to the removal of mineral mass from bridging asperities. After 1500 h the fracture aperture increased, ultimately reaching 13 μm. Apparently the dominant dissolution process switched from prop removal to etching of the void surfaces. We used X-ray CT images, digital radiographs, and fracture casts as independent methods to constrain the resulting architecture of the evolved fracture porosity, and developed a simple process-based model to examine the relative roles of asperity removal and free-face dissolution. The comparison of the model with the measurements identifies the relative importance of mass removal at fracture faces and at propping asperities. The experiments underscore the importance of dissolution in determining the sense, the rates and the magnitude of permeability-enhancement within rock fractures stimulated by chemical permeants in geothermal and petroleum reservoirs, and to a lesser degree under natural conditions pushed far-from-equilibrium.

Keywords: fracture permeability; pressure solution; free-face dissolution; geochemistry

1. Introduction

In fractured rock masses with low matrix permeability, fluid flow predominates within fractures. An

* Corresponding author. Tel./fax: +81 89 927 9853.
E-mail address: hide@dpc.ehime-u.ac.jp (H. Yasuhara).

0012-821X/$ - see front matter © 2006 Elsevier B.V. All rights reserved.
doi:10.1016/j.epsl.2006.01.046

understanding is crucial of how the flow and transport characteristics within rock fractures evolve in space and time, and is significant to many engineering or scientific applications. These include the effective recovery of targeted fluids in geothermal and petroleum reservoirs and the long-term and safe isolation of long-lived wastes in underground repositories. The influence of mechanical and chemical effects on the permeability of fractured reservoirs is well recognized, however the interaction between mechanical and chemical influences remains ill-constrained. To date, no conclusive view exists of the evolution in fracture permeability when arbitrary stresses, temperatures, and chemical potentials are applied—specifically whether permeability will increase or reduce under net dissolution. Reduction is driven as bridging asperities are removed and/or secondary minerals are reprecipitated (i.e., pressure dissolution). Increase is driven as the fracture void is etched by net dissolution (i.e., free-face dissolution). Sealing, likely driven by pressure solution, resulting from either removal of bridging asperities or mineral precipitation, is reported in some instances at elevated temperature (>300 °C) [1–5], at modest temperature (50–150 °C) [6–8], and under low effective stress (0.2 MPa) with an acidic solution [9]. Conversely, gaping driven by free-face dissolution is suggested in carbonate reservoirs, e.g., [10], and in the development of karst, e.g., [11]. Importantly, these opposing behaviors operate concurrently, but to varying degrees. Subtle changes in local conditions of applied stress, temperature or chemical potential may trigger switching between dominant mechanisms. Thus, besides monotonic sealing or gaping of a fracture, the behavior may switch, either in response to changing stress, temperature or chemical conditions, or spontaneously, with no apparent trigger [12].

This study examines changes in permeability with net dissolution that proceed within a natural fracture in Arkansas novaculite. Specifically, our focus is placed on defining the critical factors controlling the overall behavior; fracture gaping or closing. Experimental measurements of evolving fluid pressure differential between sample inlet and outlet, prescribed flow rates and confining pressure, and non-destructive CT images of the fracture, are used to constrain the evolution of fracture porosity. Final fracture void morphology is anchored by a Wood's metal cast of the fracture. These ensemble observations are used to constrain the competing processes that contribute to permeability augmentation and reduction.

2. Experimental method

The flow-through experiment was conducted on a cylindrical sample of Arkansas novaculite (50.0 mm diameter × 89.5 mm length) containing a single diametral fracture along its cylindrical axis. The fracture was split open by prying it open with a chisel, following coring. Arkansas novaculite is >99.5% quartz [13], and distilled water was used as a permeant. Thus, the chemical system was relatively simple (i.e., $SiO_2 + H_2O$). During the end-to-end flow test, the measured axial pressure differential yielded a continuous record of the averaged fracture transmissivity, that may be converted to permeability, and then to average aperture. Pre-experiment, the fracture surfaces were each profiled, and post-experiment the aperture distribution within a fracture was measured first by X-ray CT, and then by destructive casting with Wood's metal.

2.1. Experimental system

The fluid flow system configuration is shown in Fig. 1. The upper and lower rock samples were carefully mated to avoid introducing small debris within the fracture, and the mated core was confined within a Viton® sleeve and placed inside an 80-cm long tri-axial pressure cell of 9.5-cm outside diameter. Stainless-steel end plugs pierced by fluid supply tubes cap the ends of the carbon fiber-reinforced aluminum pressure cell

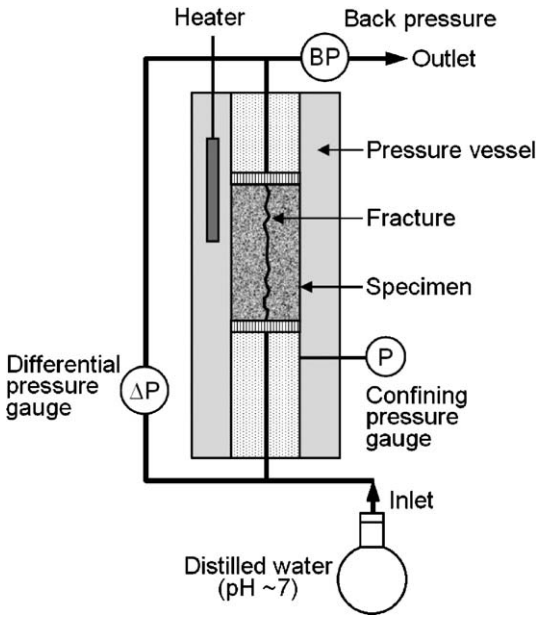

Fig. 1. Schematic illustration of experimental setup for flow-through experiment.

(Temco Inc.). Heating was by thin cylindrical electrical resistance heaters regulated to within ±2 °C by thermocouples located inside the top and the bottom parts of the coreholder. The injected fluid was preheated by cable heaters before injection through the core interior. A combination of preheating and efficient insulation maintained injected fluid temperatures congruent with those of the core specimen. The confining pressure and prescribed flow rates were established by independently controlled pressure generators. Back pressure was prescribed at 345 kPa (50 psi) by a pressure regulator located close to the outlet of the coreholder—this maintained a prescribed pore pressure at the outlet and prevented vaporization of fluid at high temperatures (>100 °C). The differential pressure between the sample inlet and outlet was recorded throughout the duration of the flow-through experiment by a pressure transducer (accurate to within ±40 Pa) exposed directly to the pore fluid.

2.2. Procedure for flow-through experiment

Constrained within the coreholder, the confining fluid was pressurized to 1.72 MPa (250 psi) resulting in a net effective stress of 1.38 MPa (200 psi) applied to the sample; the maximum differential pressure between the sample inlet and outlet is less than 0.1 MPa and the mean effective stress was maintained quasi-steady throughout the experiment. The flow-through experiment was initiated at a controlled flow rates and temperature of 1.0 mL/min, and 20 °C, and altered with progress of the test, in the range Q=1.0–0.0625 mL/min and T=20–120 °C, respectively. Experimental conditions during the entire length of the experiment (3150 h) are given in Table 1. With the fluid flow rate prescribed, differential pressure between the sample inlet and outlet was logged throughout the 3150-h duration experiment. Measured fracture transmissivity, translated to an equivalent hydraulic aperture, was evaluated from the known differential pressure, flow rate, temperature-dependent viscosity of the fluid, and the length and width of the sample, via the parallel plate approximation, e.g., [14,15].

Table 1
Experimental conditions

Time (h)	Temperature (°C)	Flow rate (mL/min)	Flow direction
0–121	20	1.0	Original
121–380	20	0.5	Original
380–858	20	0.25	Original
858–930	20	0.0	–
930–1266	20	0.25	Original
1266–1292	20	0.125	Original
1292–1494	20	0.125	Reversed
1494–1869	20	0.0625	Original
1869–2255	40	0.0625	Original
2255–2875	80	0.0625	Original
2875–3150	120	0.125	Original

2.3. Chemical analysis

Deionized water was circulated throughout the experiment. A total of 120 fluid samples were taken from the flow outlet at regular intervals (one sample per day) to determine effluent Si concentrations. Samples were assayed by inductively coupled plasma-atomic emission spectrophotometer (analytical precision within ±5%). In addition, pH was measured by a ROSS combination pH electrode (Thermo Orion) on 14 samples of the effluent, and 7 samples of the influent flux.

2.4. Roughness profilometry

Prior to the flow-through experiment the fracture was opened and both surfaces profiled for roughness [16]. These data were used to digitally reconstruct the aperture distribution for the mated fracture. The 3-D automated roughness profiling system comprises an X–Y positioning table (stroke length of 250×150 mm^2, positioning accuracy of ±15 μm, and repositioning accuracy of ±3 μm) and a 3-D laser scanner (spot dimensions of 45×20 μm^2, measurement range of ±8 mm, and maximum resolution of 0.5 μm for elevation). The maximum resolution of the 3-D laser displacement sensor is 0.5 μm in the vertical direction, but is limited by temperature variations during measurements (approximately ±5 μm error per ±2 °C). Correspondingly, vertical resolution is limited to 10 μm. Profiles (z) of the two 50.0×89.5 mm fracture surfaces were measured on a 50 μm grid in the x, y plane (horizontal), with positive-x aligned with the flow direction. Aperture distribution within the mated fracture was determined from point-by-point subtraction of the two digitized surfaces (Fig. 2), after first de-skewing the data by maintaining the mean planes of the fractures parallel.

2.5. X-ray CT imaging

Volumetric imaging of the sample was completed by X-ray CT (Universal systems Inc.) as a sequence of stacked sections orthogonal to the long-axis of core. Each slice comprises an array of 1000×1000 voxels, each defined by a single CT number. CT number is a measure of the X-ray attenuation of the voxel, and in

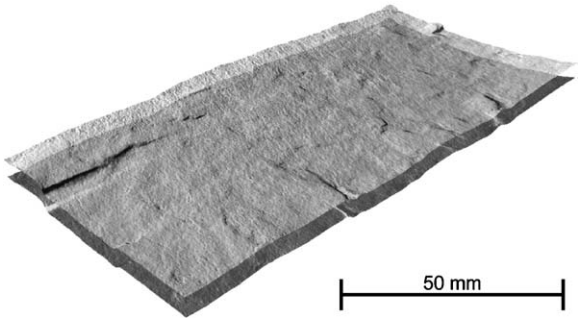

Fig. 2. Oblique view of the parallel rough surfaces digitized by the 3-D laser profilometer system.

turn depends on a combination of the density and mean atomic number of the target, and on the properties of the X-ray beam. A more detailed description on the capability and limitations of X-ray CT in core analysis may be found in Stock [34], Ketcham and Carlson [35], and Wildenschild et al. [36].

In this experiment one scanning sequence was performed after the termination of the experiment; the scanner recorded 1477 two-dimensional slices that spanned the sample, each with a thickness of 60.6 μm and an in-plane pixel resolution of 50 μm (energy level of 180 kV at 600 μA).

2.6. Wood's metal fracture casting

Fracture casting has been used to characterize the pore structure of cements and concrete [17,18], the distribution of natural fractures in coal [19], and the morphology of pore space in mudstones [20]. A fracture cast was taken at the conclusion of the experiment using Wood's metal. This alloy (50% Bi, 25% Pb, 12.5% Cd, and 12.5% Sn) has a density of 9.67 g cm^{-3}, and melts at 65.5 °C with the characteristics of a non-wetting liquid. At the conclusion of the flow-through experiment the Viton® sleeved sample was removed, end-capped, heated in an oven to 90 °C, and pressure injected with Wood's metal at 345 kPa (50 psi).

3. Experimental results and analyses

The evolution of permeability within a fracture may be attributed to the redistribution of mineral mass from contacting asperities and/or fracture void surfaces. Dissolution at the contacting asperities may result in a net-decrease in fracture aperture, provided this effect outstrips gaping induced by dissolution from the fracture surface. These dynamic processes are constrained from concurrent measurements of evolving permeability, mineral efflux, and post-experiment imaging by X-ray CT, anchored to final destructive casting of the fracture using Wood's metal.

3.1. Evolution in fracture aperture

The overall experiment is divided into two stages; the first over 1494 h at constant temperature (20 °C) but at varying flow rate (1.0–0.125 mL/min and a reversed flow of 0.125 mL/min), and the second over 1656 h at fixed flow-rate (in two sequential stages 0.0625 and 0.125 mL/min) but with stepped temperatures (20, 40, 80, 120 °C) (see Table 1). The first stage evaluates the role of flow rate, and the second the role of temperature in driving permeability changes, all as invariant confining stress (1.72 MPa).

Fig. 3a shows the evolving changes in normalized differential pressure and hydraulic aperture with time. Hydraulic aperture is evaluated from the recorded differential pressures and flow rates via the cubic law. Logged differential pressure implies the effects of prescribed flow rates and temperatures, and may be normalized to remove the influence of temperature on viscosity. Normalized differential pressure is calculated from the ratios of both flow rates and fluid viscosities between the initial and followed conditions, given by,

$$\Delta p_{\mathrm{n}} = \Delta p_{\mathrm{r}} \frac{Q_{\mathrm{i}}}{Q} \frac{\mu_{\mathrm{i}}}{\mu}, \tag{1}$$

where Δp_{n} and Δp_{r} are the normalized and recorded differential pressures, respectively. Q and μ are flow rate and dynamic viscosity of fluid, and the subscript i denotes the initial conditions (Q_{i}=1.0 mL/min and $\mu_{\mathrm{i}}=1.0\times10^{-3}$ Pa·s at 20 °C).

3.1.1. Invariant temperature test under various flow rates (0–1494 h)

The hydraulic aperture decreased monotonically from 18.5 to 10.3 μm during the first 858 h of the test, with a reduction in the flow rates from 1.0 to 0.25 mL/min. After 72 h shutdown, flow was resumed at a rate of 0.25 mL/min and the aperture slightly increased to 10.6 μm, followed by a consistent reduction in aperture. After the flow direction was reversed at 1292 h, the aperture reduced to 7.5 μm during 1292–1494 h. Abrupt decreases in fracture aperture were apparent when the flow was reversed at both 1292 and 1494 h; the measured Δp's (instead of normalized Δp) before the switching of the flow direction were 50 and 93 kPa, and rapidly increased to 65 and 108 kPa after each switching, respectively. This instantaneous closure in aperture is

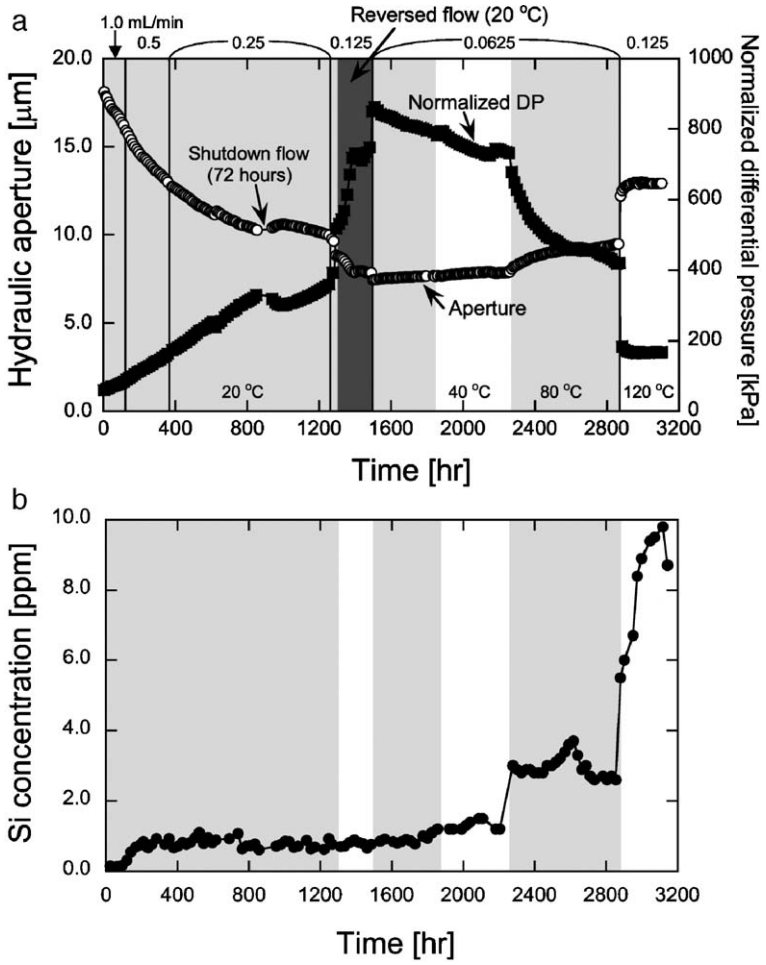

Fig. 3. Experimental measurements: (a) changes in hydraulic aperture and normalized differential pressure with time and (b) change in Si concentration with time. Measured differential pressure is normalized by the flow rates and fluid viscosities (Eq. (1)).

interpreted as a switch of the stress distribution. Effective stress at the sample inlet is smaller than that at the outlet because of the higher pore pressure applied at the inlet; this may correspondingly accommodate a larger aperture at the inlet. Switching of flow directions is correlated with the switching of stress distributions, and accordingly this may reduce aperture around the previous inlet (i.e., outlet after reverse of the flow), resulting in net-closure within the fracture.

Monotonic reduction in aperture throughout the 1494 h stage of the experiment may be attributed to the relative dominance of either mass dissolution at contacting asperities or mechanical creep of the fracture including mechanical crushing of the propping asperities due to high stress concentration, relative to that at free fracture surfaces. Both viable processes may result in an increase in average contact area within the fracture, with a consequent decrease in the rate of aperture reduction, as apparent in Fig. 3a. Although the duration of the mechanical creep is long (throughout the 1494 h stage) the contribution of crushing at the asperities and removal by dissolution cannot be ruled.

3.1.2. Fixed flow-rate test at elevated temperatures (1494–3150 h)

The hydraulic aperture continued to decrease throughout the initial 1494-h of the experiment, but monotonically increases as temperatures were elevated for the remainder of the experiment. The switch from aperture-reduction to -increase has been previously reported in carbonates [12], and the phenomenon of switching between permeability-reduction to permeability-increase is interpreted as a switch in the dominant process of mineral redistribution—from beneath the bridging asperities to the faces of the fracture. Dissolution at

contacting asperities is stress-dependent, e.g., [21,22]. The stress at the asperities decreases with an increase in contact area as the fracture closes, reducing the mass rate of removal from beneath the asperities relative to that etched by free-face dissolution. This correspondingly results in a change from net closure to net gaping, with a concomitant change in permeability.

After re-initiating flow in the original direction at 1494 h, fracture aperture slightly increased to 7.7 μm during 1494–1869 h at 20 °C. This is followed by a consistent augmentation in aperture as temperatures were elevated to 120 °C. The rates of aperture gaping increased as temperatures were raised, although this is relatively small between 20 °C (1.62×10^{-13} m/s) and 40 °C (2.31×10^{-13} m/s). This is attributed to an increase in the apparent dissolution rate with temperatures. Dissolution rates exhibit an Arrhenius-type dependence on temperature, e.g., [23,24], given by,

$$k_+ = k_+^0 \exp(-E_{k_+}/RT) \tag{2}$$

where k_+ is dissolution rate constant. k_+^0 and E_{k_+} are pre-exponential factor and activation energy, respectively (k_+^0=1.59 mol m^2 s^{-1} and E_{k_+}=71.3 kJ mol^{-1} for quartz [23]). R is the gas constant and T is temperature. The dissolution rate constant at 120 °C is three orders of magnitude larger than that at 20 °C, explaining the observed growth in aperture evolution rate.

3.2. Surface dissolution

The change in measured effluent Si concentration is shown in Fig. 3b. Corresponding pH magnitudes are shown in Table 2, and vary slightly from inlet to outlet, with average values of 7.06 and 6.92, respectively. The distilled water was supplied from the same distiller throughout the experiment, although the slight variation in pH measured at the inlet is due variability in the output of the unit. Concentrations measured at 20 °C were in the range 0.13 to 1.20 ppm with a mean of 0.76 ppm, and showed slight fluctuation through this stage. The mean values at elevated temperatures increased with the increase of temperature; their values at 40, 80, and 120 °C were 1.30, 2.96, 8.10 ppm, respectively. Measured Si concentrations are clearly temperature dependent, and show the Arrhenius-type dependence (Fig. 4). The activation energy of Si solubility is reported by Iler [25] at 21.7 kJ mol^{-1}, and this value is close to that determined from measurements in this study (22.2 kJ mol^{-1}). In contrast, the measured concentrations are much lower than Si solubilities

Table 2
pH measured from inlet and outlet samples

Time (h)	Inlet pH	Outlet pH
19	6.25	6.41
68	–	6.11
259	–	6.32
427	6.69	6.34
595	–	6.34
616	7.26	–
764	–	6.39
1076	–	7.98
1123	7.18	–
1221	–	7.83
1366	–	7.36
1680	–	7.00
1819	8.21	–
2326	–	7.72
2585	6.97	–
2627	–	6.62
2825	6.85	–
2831	–	7.35
2974	–	7.15
Ave.	7.06±0.42	6.92±0.52

(~9, 17, 44, 94 ppm at 20, 40, 80, 120 °C, respectively [25]) due to the short residence time of the fluid within the fracture (ca. a few tens of seconds). This implies that precipitation remained inactive within the fracture throughout the 3150 h duration of the experiment, and suggests that net dissolution prevailed throughout.

The role of dissolution at contacting asperities has been examined in terms of the rate of aperture reduction, db/dt, [7,26] recorded from flow-through tests where independent estimates of the hydraulic fracture aperture are derived from the effusing fluid and mineral flux. Hydraulically measured aperture reduction rates, db/dt, in the first 858-h duration are in the range 2.0×10^{-11} to 5.0×10^{-13} m/s as shown in Fig. 5. The hydraulically measured rates may be augmented by estimates from mineral mass efflux, where an assumption is made regarding the contact-area ratio, R_c, as,

$$\frac{db}{dt} = \frac{Q\cdot C_{SiO_2}}{R_c\cdot A_f \rho_g} \tag{3}$$

where A_f is the total fracture area (A_f=8.95×10^{-3} m^2) and ρ_g is grain density (2650 kg m^{-3} for quartz). Varying the unmeasured fractional contact area in the range 1% to 30%, the rates of aperture reduction, db/dt, may be determined from the mean Si concentrations, C_{Si}, of 0.18, 0.77, and 0.87 ppm, equivalent to SiO_2 concentration, C_{SiO_2}, of 0.39, 1.63, and 1.86 ppm, at prescribed flow rates, Q, of 1.0, 0.5, and 0.25 mL/min,

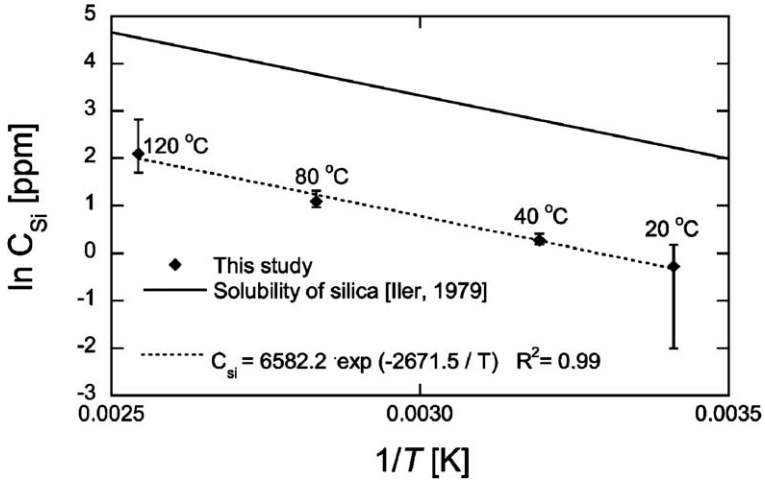

Fig. 4. Relation between Si concentration and temperature. Solid dots represent mean measured concentrations and error bars show the maximum and minimum concentrations at the temperatures. Measured Si concentration is strongly correlated to temperature by an Arrhenius-type relation. Solid line represents the solubility curve by Iler [25]. with activation energy of 21.7 kJ mol^{-1}, and dotted line is the regression curve for the measured with apparent activation energy of 22.2 kJ mol^{-1}.

respectively. These estimates, in the range 1.1×10^{-10} to 2.0×10^{-12} m/s, are close to, but slightly higher than those recovered from the hydraulic measurements. This mismatch may result either from an unaccounted contribution of dissolution at the fracture void walls, or from an underestimate of assumed fracture contact area. If crushing beneath asperities and subsequent removal by dissolution does contribute to the observed response, this response would be of similar form to that observed—i.e., a rapid initial closure, followed by a slowing in closure as the contact area builds and the driving stress drops.

3.3. X-ray CT analysis

Non-invasive imaging was used to evaluate the 3D structure of the fracture surfaces. The left side of Fig. 6 shows two CT images taken at the termination of the flow experiment from the upper (a) and lower (b) parts of the rock sample. The fracture is clearly visible in the

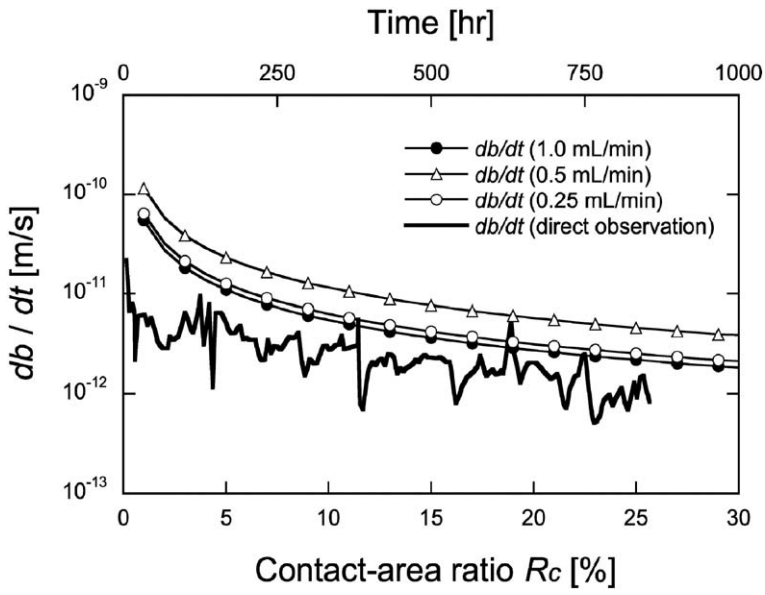

Fig. 5. Comparison of change in rate of aperture reduction, db / dt. Solid line represents the change in direct observation of db / dt with time (0–858 h). Solid circles, open triangles, and open circles represent predictions by Eq. (3) at different flow rates in the range of 1.0 to 0.25 mL/min.

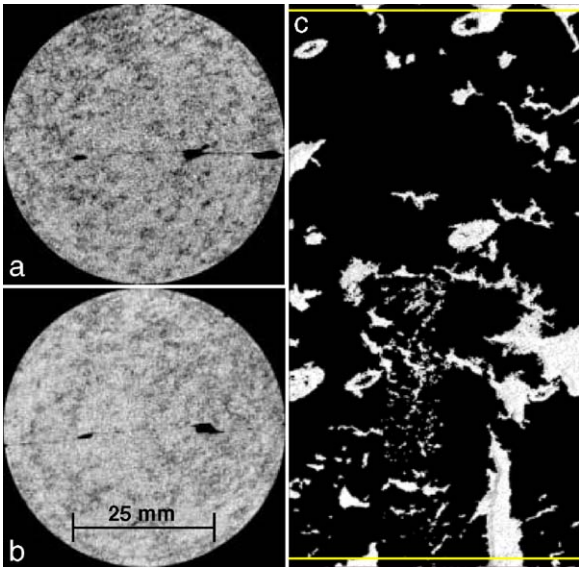

Fig. 6. Images of the CT scan obtained at the end of the flow experiment. The left images show two CT images of the rock sample taken at the top (a) and bottom (b) parts of the sample. The fracture is clearly visible at the center of the image where the large black pores are areas where pieces of the fracture surface was missing. The right image (c) shows a 3D reconstruction of 1477 CT images representing a complete view of the fracture surface. The white areas are fracture voids demarked with a threshold CT number of 2650.

center of the image (marked in black). Some of the large black areas are places where pieces of rock are missing likely due to mechanical brakeage prior to the start of the experiment. The black spots in the rocks matrix are areas where the density of the rock is lower relative to the rest of the matrix. These regions are not interconnected and exert no influence on the in-fracture flow. The right side of Fig. 6 shows a 3D reconstruction of 1477 images representing a complete view of the rock fracture. The two yellow lines demark the scans where two images shown on the left were captured. The white regions in the 3D reconstruction are fracture voids demarked with a threshold CT number of 2650 that was chosen by trial and error to characterize the fracture plane in an optimal way. The 3D reconstruction suggests that there are no continuous paths within the fracture, however this aberration results from the finite resolution of the imaging ($50 \times 50 \times 60.6$ μm). By counting the number of pixels that have a CT number lower than the chosen threshold of 2650 and multiplying them by the size of each pixel ($50 \times 50 \times 60.6$ μm), we may calculate the total volume of the fracture (white area) and estimate the average fracture aperture of the whole rock sample. The total fracture volume was calculated to be 390 mm^3 (2,563,798 pixels), which for the scanned area of 4200 mm^2 gives an average fracture aperture of 95 μm. The average fracture aperture estimated from the CT images is larger than the hydraulic aperture at the end of experiment (i.e., 13 μm), which may be attributed to the chosen threshold CT number; the larger the prescribed threshold, the larger the resulting void volume and aperture. However, the estimated aperture hereinabove is still plausible and indexes to the actual value evaluated from the flow-through experiment although the CT resolution is insufficiently high.

3.4. Extraction of Wood's metal fracture

Following the injection of Wood's metal, the impregnated rock sample was re-imaged by X-ray CT. The clarity of imaging is limited by the very high density of the Wood's metal alloy (9.67 g cm^{-3}) and by beam guiding in the dense fracture plane. Alternatively, Fig. 7 shows two digital radiographs (DR) of the rock sample. The white regions are voids filled with Wood's metal. The left image shows a plan view of the fracture that depicts no continuous flow paths along the fracture plane, similar to the 3D reconstruction by the X-ray CT (Fig. 6). The side view on the right image indicates that the fracture has a measurable but unquantified thickness, and is continuous through the sample, implying that Wood's metal penetrated through most of the fracture.

The Wood's metal cast was removed from the novaculite by first trimming the sample to close to the fracture, and then immersing the remaining ingot inside

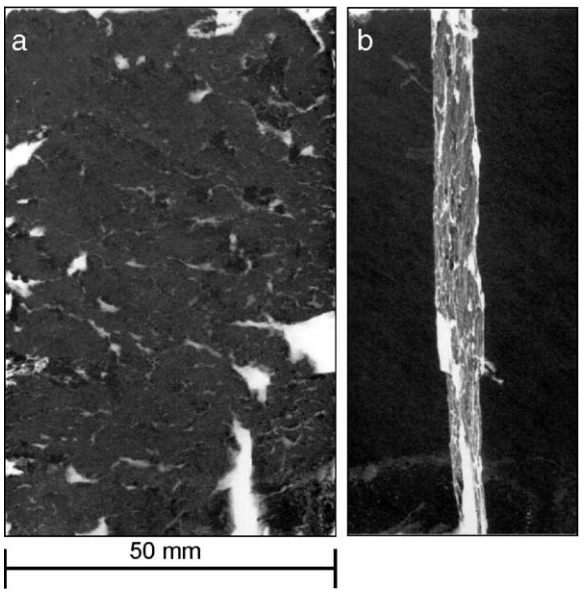

Fig. 7. A digital radiograph (DR) of the fracture cast of Wood's metal: (a) plane view and (b) side view. The white areas represent the filled pores.

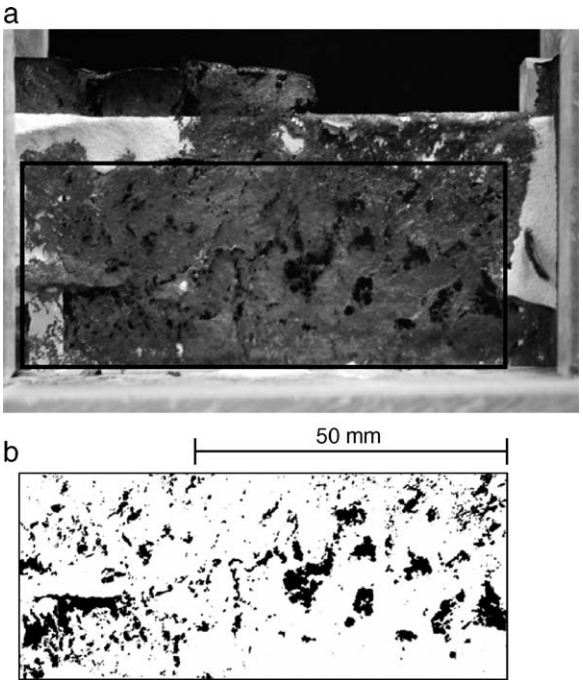

Fig. 8. Wood's metal fracture extracted through chemical dissolution using hydrofluoric acid: (a) whole fracture—white region is residual rock sample, and (b) black-and-white representation of the boxed area in (a). Black area represents regions in contact and calculated contact area is 14.5%.

a bath filled with hydrofluoric acid (~25 wt.%). Immersion for 166 h removed the surrounding rock matrix, although a small portion of the fracture top was bowed (Fig. 8a). It is apparent that Wood's metal propagated throughout the fracture except not into the regions in contact. No preferential flow paths are apparent within the cast, which is congruent with the CT and DR observations. Importantly, the alloy fracture cast enables the contact area to be quantitatively evaluated from the digitized black-and-white image (~65% of the whole fracture) as shown in Fig. 8b. The calculated contact-area ratio is 14.5% and may be consistent with the plausible amount in rock fractures, e.g., [15,27].

4. Process-based model

A process-based model is presented to describe the evolution of fracture aperture mediated by the competing processes of dissolution at contacting asperities (the most viable process that reduces a fracture aperture) and at fracture walls. The model is applied to examine the experimental observations—a net-reduction in aperture switched to a net-increase with the application of heating. The model is a diagnostic representation because the observed mineral efflux is used as input data, but is capable of deconvolving the relative dominance of the dissolution processes, which is not apparent from the raw experimental measurements of changes in the hydraulic aperture and the mineral concentration. Also, this enables the rates and magnitudes of aperture changes to be followed with time from a mechanistic standpoint.

4.1. Relation between fracture aperture and contact area

The dissolution processes irreversibly alters the geometry of the contacting fracture surfaces, requiring that the initial fracture geometry be identified. For this, a simple relation between the mean fracture aperture and contact-area ratio is determined using images of two rough surfaces digitized by the 3-D roughness profiling system. Fig. 9 shows the relation between the mean mechanical aperture, $<b>$, and the contact-area ratio, R_c. The mean aperture is defined as the arithmetic average aperture obtained by the point-by-point subtraction between the two digitized surfaces (negative values resulting from subtraction are set to be zero in the local aperture). The contact-area ratio is merely defined by the ratio of the number of equally spaced profile points representing interpenetrated surfaces, to the total number of measurement points. The relation shows exponential decay of fracture aperture as the contact area increases. Note that this aperture configuration is a numerical product, not equivalent to the physically realistic aperture constrained under the experimental conditions, although they may be comparable to each other. Actually, it is impossible for the digitally reconstructed fracture to replicate the physical one under experimental conditions because the mating of the real surfaces may result in block rotations and a resulting skewing in the aperture data. Correspondingly, the digitized surface data were de-skewed by maintaining the mean planes of the fractures parallel. Point-by-point subtraction was then used to determine the equivalent physical fracture, to a first-order approximation.

4.2. Constitutive relations

The digitized fracture, obtained from profilometry, constrains the relation between the fracture aperture and the contact-area ratio as shown in Fig. 9. This relation is approximated by the regression curve, given by [26],

$$\langle b\rangle = b_r + (b_0 - b_r)\exp(-(R_c - R_{c0})/a), \quad (4)$$

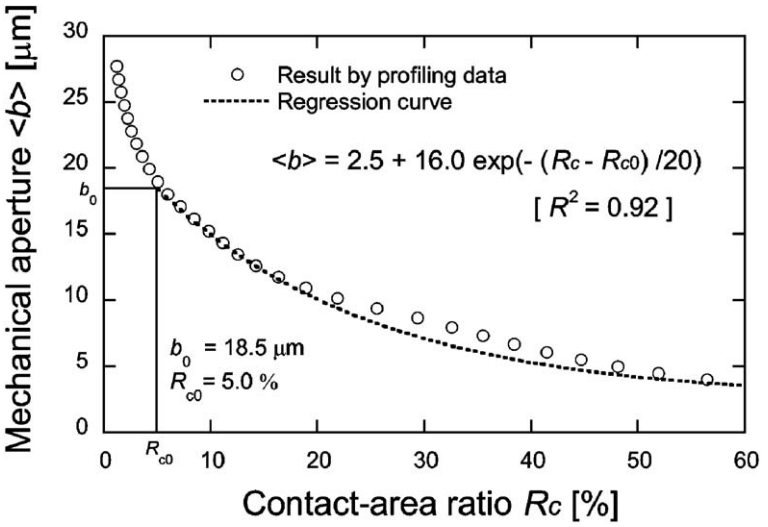

Fig. 9. Relation between mean aperture and contact-area ratio. Circles are evaluated from point-by-point subtraction using the profiling data, and the dotted line is the regression curve of $\langle b\rangle = 2.5 + 16.0\ \exp(-(R_c - R_{c0})/20)$ with the correlation coefficient, $R^2 = 0.92$.

where $\langle b\rangle$, b_r, and b_0 are the mean mechanical, residual and initial apertures, respectively. R_c is the contact-area ratio, and a is a constant. The initial aperture is set to be 18.5 μm because the hydraulic aperture evaluated from the flow-through experimental measurements started initially with this value. Although these mechanical and hydraulic apertures may not be equivalent [28–30], reckoning them as equivalent is reasonable to a first-order approximation. The regression analysis obtained in Fig. 9 shows the residual and initial apertures to be 2.5 and 18.5 μm, respectively.

The evolution of fracture aperture incorporates the combined effects of asperity interpenetration (decrease in aperture) and of free-face etching (increase in aperture). Precipitation may also influence hydraulic behavior, but the short residence times reflected in the observed undersaturation of the circulating fluid to Si suggests that precipitation will exert a minor influence. Consequently the effects of precipitation are not considered.

In defining effusing mass, it is convenient to consider the dissolved mass flux, $\mathrm{d}M/\mathrm{d}t$, evaluated from prescribed flow rates and measured quartz concentrations, given as,

$$\frac{\mathrm{d}M}{\mathrm{d}t} = QC_{\mathrm{SiO_2}}. \tag{5}$$

The relative contributions of dissolution at contacting asperities and fracture void walls to the evolution in fracture aperture may be deconvolved and quantified by applying an arbitrary ratio of mass sourced from either contact area or free surface over total dissolved mass, defined by,

$$V^{\mathrm{C}}_{t+\Delta t} = V^{\mathrm{C}}_{t} + \left(\frac{\mathrm{d}M}{\mathrm{d}t}\frac{\Delta t}{\rho_{\mathrm{g}}}\right) r_{\mathrm{C}}, \tag{6}$$

$$V^{\mathrm{F}}_{t+\Delta t} = V^{\mathrm{F}}_{t} + \left(\frac{\mathrm{d}M}{\mathrm{d}t}\frac{\Delta t}{\rho_{\mathrm{g}}}\right) r_{\mathrm{F}}, \tag{7}$$

where V^{C}_{τ} and V^{F}_{τ} represent the volume dissolved from contacting asperities and free fracture wall at $t=\tau$, respectively. r_{C} and r_{F} are ratios of mass fluxes sourced from contact area and free surface area over total mass efflux, respectively, which results in $r_{\mathrm{C}}+r_{\mathrm{F}}=1$. The volume dissolved from the contact area during the infinitesimal time interval, $\mathrm{d}t$, is given by,

$$\mathrm{d}V^{\mathrm{C}}_{t} = WLR_{\mathrm{c}}|_{t}\mathrm{d}u, \tag{8}$$

where W and L are the width (50.0 mm) and the length (89.5 mm) of novaculite sample, respectively. $\mathrm{d}u$ represents change in displacement driven by dissolution at contact area during $\mathrm{d}t$. The relation between the mechanical aperture, $\langle b\rangle$, and displacement, u, can be defined by,

$$\mathrm{d}u = -\frac{d\langle b\rangle}{1-R_{\mathrm{c}}|_{t}}, \tag{9}$$

because $\langle b\rangle$ is the arithmetic average of the local apertures with contacting asperities (the negative sign is due to the fact that the aperture reduces by dissolution).

Substituting this into Eq. (8), the cumulative volume dissolved from contact area can be evaluated by integrating Eq. (8) using Eq. (4) with respect to the contact-area ratio, as,

$$\begin{aligned} V^{\mathrm{C}}_{t+\Delta t} &= -WL\int_{R_{c0}}^{R_{c|_{t+\Delta t}}} \frac{R_c|_t}{1-R_c|_t}\frac{\mathrm{d}\langle b\rangle}{\mathrm{d}R_c}\mathrm{d}R_c \\ &= (b_0-b_r)WL\exp\left(-\left(1+R_c|_{t+\Delta t}\right)/a\right) \\ &\quad\times\left[\exp\left((1+R_{c0})/a\right)-\exp\left(\left(1+R_c|_{t+\Delta t}\right)/a\right)\right. \\ &\quad+\exp\left(\left(R_{c0}+R_c|_{t+\Delta t}\right)/a\right)/a\left(\mathrm{Ei}\left((1-R_{c0})/a\right)\right. \\ &\quad\left.\left.-\mathrm{Ei}\left(\left(1-R_c|_{t+\Delta t}\right)/a\right)\right)\right] \end{aligned} \tag{10}$$

where $\mathrm{Ei}(x)$ is the exponential integral function and for the positive value of x the function is expressed using the Puiseux series [31], as,

$$\mathrm{Ei}(x) = \gamma + \ln x + \sum_{n=1}^{\infty}\frac{x^n}{n!n}, \tag{11}$$

where $\gamma(=0.5772...)$ is the Euler–Mascheroni constant. Consequently, Eq. (10) is rearranged as,

$$\begin{aligned} V^{\mathrm{C}}_{t+\Delta t} &= (b_0-b_r)WL\exp\left(-\left(1+R_c|_{t+\Delta t}\right)/a\right) \\ &\quad\left[\exp\left((1+R_{c0})/a\right)-\exp\left(\left(1+R_c|_{t+\Delta t}\right)/a\right)\right. \\ &\quad+\exp\left(\left(R_{c0}+R_c|_{t+\Delta t}\right)/a\right)/a \\ &\quad\left.\times\left(\ln\frac{1-R_{c0}}{1-R_c|_{t+\Delta t}}+\sum_{n=1}^{\infty}\frac{(1-R_{c0})^n-(1-R_c|_{t+\Delta t})^n}{a^n n!n}\right)\right] \end{aligned} \tag{12}$$

Substituting this into Eq. (6), the contact-area ratio is updated, and the average fracture aperture mediated by dissolution at contacting asperities is also evaluated using Eq. (4), given as,

$$\langle b\rangle_c|_{t+\Delta t} = 2.5 + 16.0\exp\left(-\left(R_c|_{t+\Delta t}-R_{c0}\right)/20\right), \tag{13}$$

where $\langle b\rangle_c|_{t+\Delta t}$ denotes the updated fracture aperture mediated by dissolution at contacting asperities, which does not include the contribution of free-face dissolution. The effect is evaluated from Eq. (7). The volume dissolved from the fracture void walls is given by,

$$V^{\mathrm{F}}_{t+\Delta t} = \langle b\rangle_{\mathrm{F}}|_{t+\Delta t}WL, \tag{14}$$

where $\langle b_{\mathrm{F}}\rangle|_{t+\Delta t}$ represents the change in aperture due to free-face dissolution at $t=t+\Delta t$. Substituting this equation into Eq. (7), yields $\langle b_{\mathrm{F}}\rangle|_{t+\Delta t}$. Note that the process of dissolution at the free surfaces assumes no contribution to changes in contact-area ratio and displacement, and merely augments the volume of fracture void. Finally, the average fracture aperture at $t=t+\Delta t$ is defined as,

$$\langle b\rangle|_{t+\Delta t} = \langle b\rangle_c|_{t+\Delta t} + \langle b\rangle_{\mathrm{F}}|_{t+\Delta t}, \tag{15}$$

where $\langle b\rangle|_{t+\Delta t}$ denotes the average fracture aperture at $t=t+\Delta t$. The iterative procedure is employed to march through time.

4.3. Replicating experimental measurements

The evolution in the fracture aperture is followed in time using the model presented in Section 4.2. Dissolution mass fluxes, $\mathrm{d}M/\mathrm{d}t$, are evaluated from Eq. (5) at six different stages as shown in Fig. 10; stages I, II, and III represent the early isothermal experiment at 20 °C with the experimental period divided to pre-reverse (stage I), reversed (stage II), and post-reverse (stage III) flow stages. And stages IV, V, and VI are the 40, 80, and 120 °C experiments, respectively. To follow the experimental measurements of aperture change, the unmeasured, but necessary parameters of r_{C} and r_{F} in Eqs. (6) and (7) are prescribed arbitrarily at each stage. During the experiments, two sharp reductions in aperture resulted from the reversing of the flow direction at 1292 and 1494 h. This is followed by resetting the aperture according to that measured in the experiment and the contact-area ratio is updated using Eq. (4).

Predicted changes in fracture aperture and normalized differential pressure evaluated from the cubic law are shown in Fig. 11, together with the experimental measurements. Predictions show good agreement with the measurements when the unknown magnitudes of r_{C} and r_{F} are suitably prescribed; $r_{\mathrm{C}}=0.59$ and $r_{\mathrm{F}}=0.41$ in stage I, $r_{\mathrm{C}}=1.0$ and $r_{\mathrm{F}}=0.0$ in stage II, and $r_{\mathrm{C}}=0.0$ and $r_{\mathrm{F}}=1.0$ in stages III–VI. In stage I the fracture aperture monotonically decreases with time. As shown in Fig. 12, the prediction shows that the contact-area ratio increases up to ~28% in stage I. The relatively smaller contact area amplifies the rate of aperture reduction over the increase produced by etching of the open fracture (~72%). This results in an observable net-decrease in aperture. In stage II $r_{\mathrm{C}}=1.0$ and $r_{\mathrm{F}}=0.0$ are prescribed to maximize the rate of aperture decrease. However, the rates measured in the experiment are still higher than those predicted (apparent in Fig. 11b). Also, it is difficult to understand why no dissolution at the fracture void surfaces proceeds despite the severe undersaturation in Si; the average Si concentration measured in stage II is 0.77 ppm, whereas the Si solubility at 20 °C is ~9 ppm [25]. This discrepancy between the experiment and the prediction may be interpreted as non-accommodated mechanisms such as mechanical creep and

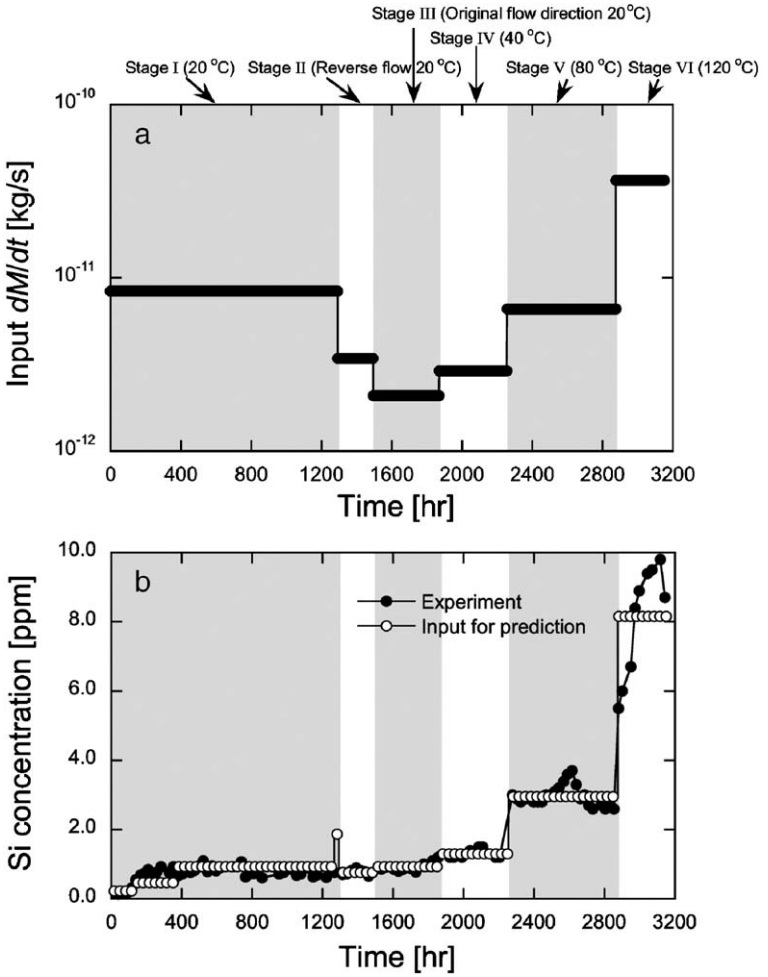

Fig. 10. Input data for prediction; (a) the average dissolution mass fluxes at six different stages evaluated from the measured Si concentrations and prescribed flow rates and (b) comparison of Si concentrations with time between the experiment and the inversely calculated using the input of dissolution mass fluxes.

crushing of propping asperities and crushed debris clogging flow-path, resulting in the sharp increase of impedance. In stages III to VI the fracture aperture consistently increases as dissolution proceeds. Significantly, the model simulations show that dissolution at contacting asperities may not occur throughout these stages, rather than that the etching process dominates over the minor effect of aperture reduction due to dissolution at contacting asperities. Rates of dissolution at contacting asperities decrease as the contact area grows, and will effectively halt when stress acting on contact area reaches a critical stress [32,33,26]. Abrupt decreases of aperture were measured immediately after the switching of the flow direction in stage II. This mechanical effect of the destruction of contacting bridges enlarges overall contact-area ratio, and thus the contact stresses may fall below some critical stress, leading to inactive dissolution at contacting asperities during stages III to VI.

The ultimate contact area that has evolved by the end of the 3150-h test is predicted to be ~34% as shown in Fig. 12, and overestimates that measured by Wood's metal impregnation (14.5%). This is attributed to the overly simple representation of the relation between fracture aperture and contact area (i.e., Eq. (4) and Fig. 9), which is incapable of representing the spatially distributed change in aperture resulting from spatial conditions of flow, stress, and chemistry. The occurrence of clogging (aperture reduction) without an increase in contact area may be triggered by local precipitation, which is not accommodated in the current model. This implicates that further topographical constraints of two rough surfaces in contact are needed to accommodate a spatial complexity of flow, stress, and

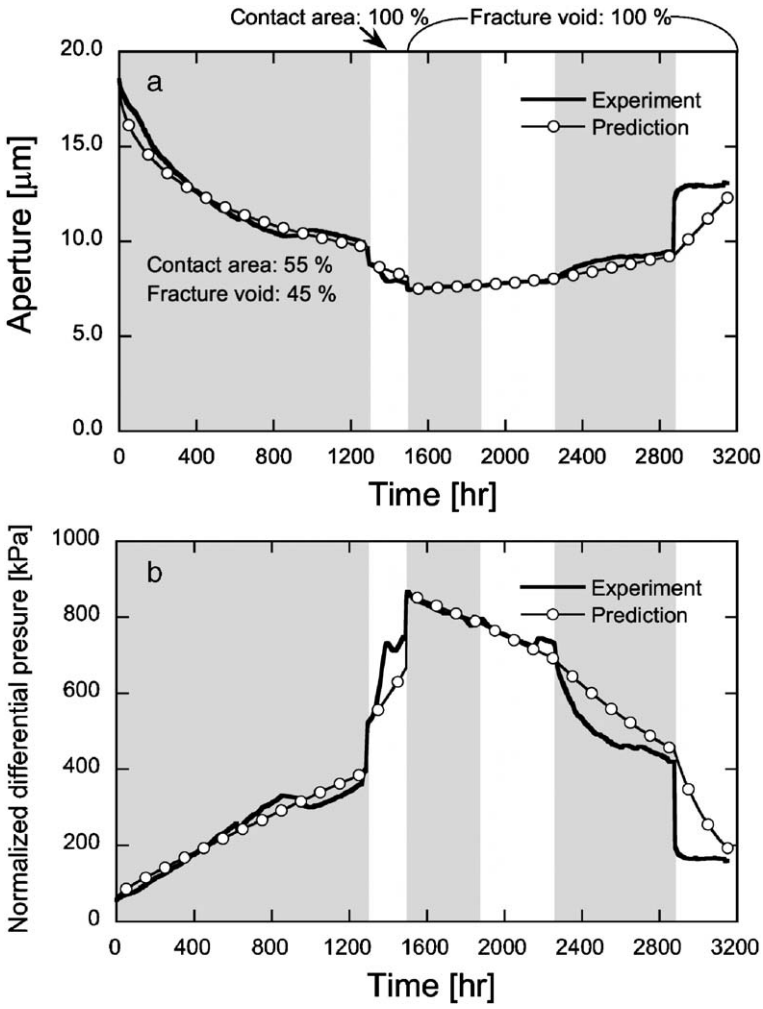

Fig. 11. Comparisons of changes in (a) aperture and (b) normalized differential pressure with time between experimental results and predictions. Solid line represents the experiments, and open circles are predictions with appropriately applied ratios of r_C and r_F.

chemistry and to achieve a more realistic understanding of the evolution in fracture aperture.

5. Conclusions

Experimental measurements of fluid and mineral mass effluxes, constrained by non-destructive imaging by X-ray CT and digital radiography, and by destructive imaging of a fracture cast, allow the evolution of fracture aperture to be followed. For isothermal flow at low temperature (20 °C), the fracture closed monotonically as the bridging asperities are progressively removed. This amounts to a 60% reduction in fracture aperture over the initial 1500 h duration of the experiment. Subsequently, free-face dissolution dominates over the effects of dissolution at contacting asperities, and results in an augmentation in fracture aperture. The rate of gaping increases with an increase in temperature, corresponding to the exponential (or Arrhenius-type) dependence on the mineral effluxes measured. The activation energy constrained in this work is 22.2 kJ mol^{-1}, congruent with that obtained from Iler [25] (i.e., 21.7 kJ mol^{-1}).

The post-experiment observations by the X-ray CT, digital radiograph, and Wood's metal cast revealed the detailed distribution of local apertures and regions in contact within the fracture. The three independent measurements imply no presence of a preferential flow path generated during the experiments. The average aperture evaluated from the CT images is sevenfold larger than the hydraulic aperture at the end of the experiment. This mismatch is likely due to limitations in the resolution of the CT imaging, and in the choice of threshold CT number.

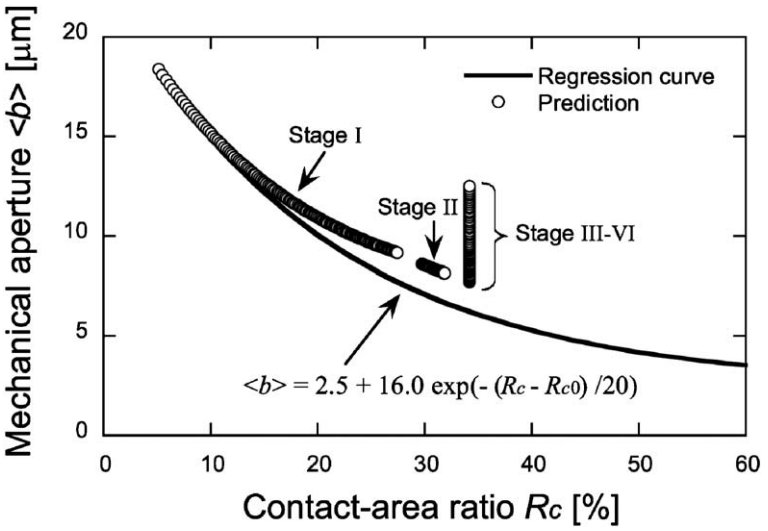

Fig. 12. Predicted progress in fracture aperture with contact-area ratio. In stages I and II the contact-area ratio monotonically increases with decrease of aperture due to dominant process of dissolution at contacting asperities, whereas in stages III to VI dissolution at free fracture wall controls net-dissolution and enlarges void space without increase of contact area.

A process-based model is applied to examine the experimental observations—that aperture closure switches to aperture growth, but all the time due to net mineral dissolution. Employing a simple relation between fracture aperture and contact-area ratio, and assigning the sources of mineral dissolution evaluated from measured Si concentrations to contact area and free void walls with certain ratios, the model is capable of following the rates and magnitudes of aperture changes measured in the experiment. However, the ultimate contact area predicted significantly overestimates that constrained by the profile of a Wood's metal cast of the fracture.

The measured Si concentrations are significantly below equilibrium solubilities at all temperatures, due to the high prescribed flow rates, and the resulting short residence time in the fracture. Examining this far-from-equilibrium behavior is important in considering the rates and magnitudes of permeability-enhancement within rock fractures stimulated by chemical permeants in geothermal and petroleum reservoirs. The current experimental measurements showed permeability degradation first and then enhancement with the increased rates with an increase in temperature, but the important factors (i.e., temperature, stress, and chemistry in the pore fluid) triggering this switching remain insufficiently constrained (moreover, it is uncertain whether such switching will occur under in situ conditions that applied temperatures, stresses, and fluid chemistries within fractured rock masses of interest may be in quasi-steady state before hydraulic and chemical stimulation). Thus, further detailed investigations are required to achieve more realistic understanding on the evolution in fracture permeability mediated by coupled thermal, hydraulic, mechanical, and chemical processes.

Acknowledgements

This work has been supported by grants DOE-BES-DE-FG02-00ER15111, DOE-DE-PS26-01NT41048, DOE-DE-FG36-04GO14289, and ARC DP0209425. This support is gratefully acknowledged. The comments of two anonymous reviewers significantly contributed to the quality of the final manuscript.

References

[1] D.E. Moore, D.A. Lockner, J.D. Byerlee, Reduction of permeability in granite at elevated temperatures, Science 265 (1994) 1558–1561.
[2] K. Kanagawa, S.F. Cox, S. Zhang, Effects of dissolution–precipitation processes on the strength and mechanical behavior of quartz gouge at high-temperature hydrothermal conditions, J. Geophys. Res. 105 (B5) (2000) 11,115–11,126.
[3] C.E. Morrow, D.E. Moore, D.A. Lockner, Permeability reduction in granite under hydrothermal conditions, J. Geophys. Res. 106 (2001) 30,551–30,560.
[4] E. Tenthorey, S.F. Cox, H.F. Todd, Evolution of strength recovery and permeability during fluid–rock reaction in experimental fault zones, Earth Planet. Sci. Lett. 206 (2003) 161–172.
[5] C. Higlers, E. Tenthorey, Fracture sealing of quartzite under a temperature gradient: experimental results, Terra Nova 16 (4) (2004) 173–178.
[6] W. Lin, J. Roberts, W. Glassley, D. Ruddle, Fracture and matrix permeability at elevated temperatures, Workshop on significant

issues and available data, Near-field/Altered-zone coupled effects expert elicitation project, San Francisco, 1997 November.
[7] A. Polak, D. Elsworth, H. Yasuhara, A. Grader, P. Halleck, Permeability reduction of a natural fracture under net dissolution by hydrothermal fluids, Geophys. Res. Lett. 30 (20) (2003) 2020, doi:10.1029/2003GL017575.
[8] P.F. Dobson, T.J. Kneafsey, E.L. Sonnenthal, N. Spycher, J.A. Apps, Experimental and numerical simulation of dissolution and precipitation: implications for fracture sealing at Yucca Mountain, Nevada, J. Contam. Hydrol. 62–63 (2004) 459–476.
[9] W.B. Durham, W.L. Bourcier, E.A. Burton, Direct observation of reactive flow in a single fracture, Water Resour. Res. 37 (2001) 1–12.
[10] X. Liu, A. Ormond, K. Bartko, Y. Li, P. Ortoleva, A geochemical reaction-transport simulator for matrix acidizing analysis and design, J. Pet. Sci. Eng. 17 (1997) 181–196.
[11] A.N. Palmer, Origin and morphology of limestone caves, Geol. Soc. Am. Bull. 103 (1991) 1–21.
[12] A. Polak, D. Elsworth, J. Liu, A.S. Grader, Spontaneous switching of permeability changes in a limestone fracture with net dissolution, Water Resour. Res. 40 (2004) W03502, doi:10.1029/2003WR002717.
[13] V.W. Lee, S.J. Mackewell, S.L. Brantley, The effect of fluid chemistry on wetting textures in novaculite, J. Geophys. Res. 96 (B6) (1991) 10023–10037.
[14] A.F. Gangi, Variation of whole and fractured porous rock permeability with confining pressure, Int. J. Rock Mech. Min. Sci. Geomech. Abstr. 15 (1978) 249–257.
[15] Y.W. Tsang, P.A. Witherspoon, Hydromechanical behavior of a deformable rock fracture subject to normal stress, J. Geophys. Res. 86 (1981) 9287–9298.
[16] Y. Mitani, T. Esaki, G. Zhou, Y. Nakashima, Experiments and simulation of shear-flow coupling properties of a rock joint, in: P.J. Culligan, H.H. Einstein, A.J. Whittle (Eds.), Proc. 39th US Rock Mech. Symp. Cambridge, 2003, pp. 1459–1464.
[17] A.B. Abell, K.L. Willis, D.A. Lange, Mercury intrusion porosimetry and image analysis of cement-based materials, J. Colloid Interface Sci. 211 (1999) 39–44.
[18] K.M. Nemati, Preserving microstructure of concrete under load using the Wood's metal technique, Int. J. Rock Mech. Min. Sci. 37 (2000) 133–142.
[19] C.D. Montemagno, L.J. Pyrak-Nolte, Fracture network versus single fractures: measurement of fracture geometry with X-ray tomography, Phys. Chem. Earth, A 24 (7) (1999) 575–579.
[20] A. Hildenbrand, J.L. Urai, Investigation of the morphology of pore space in mudstones—first results, Mar. Pet. Geol. 20 (2003) 1185–1200.
[21] E.H. Rutter, The kinetics of rock deformation by pressure solution, Philos. Trans., R. Soc. Lond., Ser. A 283 (1976) 203–219.
[22] R. Raj, Creep in polycrystalline aggregates by matter transport though a liquid phase, J. Geophys. Res. 87 (B6) (1982) 4731–4739.
[23] J.D. Rimstidt, H.L. Barnes, The kinetics of silica–water reactions, Geochim. Cosmochim. Acta 44 (1980) 1683–1699.
[24] P.M. Dove, D.A. Crerar, Kinetics of quartz dissolution in electrolyte solutions using a hydrothermal mixed flow reactor, Geochim. Cosmochim. Acta 54 (1990) 955–969.
[25] R.K. Iler, The Chemistry of Silica, John Wiley, New York, 1979.
[26] H. Yasuhara, D. Elsworth, A. Polak, Evolution of permeability in a natural fracture: Significant role of pressure solution, J. Geophys. Res. 109 (2004) B03204, doi:10.1029/2003JB002663.
[27] L.J. Pyrak-Nolte, L. Myer, N.G.W. Cook, P.A. Witherspoon, Hydraulic and mechanical properties of natural fractures in low permeability rock, Proc. Int. Cong. Int. Soc. Rock Mech. Montreal, 1987, pp. 225–231.
[28] P.A. Witherspoon, J.S.Y. Wang, K. Iwai, J.E. Gale, Validity of cubic law for fluid flow in a deformable rock fracture, Water Resour. Res. 16 (1980) 1016–1024.
[29] A.R. Piggott, D. Elsworth, Laboratory assessment of the equivalent apertures of a rock fracture, Geophys. Res. Lett. 30 (13) (1993) 1387–1390.
[30] C.E. Renshaw, On the relationship between mechanical and hydraulic apertures in rough-walled fracture, J. Geophys. Res. 100 (1995) 24,629–24,636.
[31] H. Jeffreys, B.S. Jeffreys, Methods of mathematical physics, Cambridge University Press, Cambridge, England, 1988, pp. 470–472.
[32] A. Revil, Pervasive pressure-solution transfer: a poro-visco-plastic model, Geophys. Res. Lett. 26 (2) (1999) 255–258.
[33] H. Yasuhara, D. Elsworth, A. Polak, A mechanistic model for compaction of granular aggregates moderated by pressure solution, J. Geophys. Res. 108 (B11) (2003) 2530, doi:10.1029/2003JB002536.
[34] S.R. Stock, X-ray microtomography of materials, Int. Mater. Rev. 44 (4) (1999) 141–164.
[35] R.A. Ketcham, W.D. Carlson, Acquisition, optimization and interpretation of X-ray computed tomographic imagery: applications to the geosciences, Comput. Geosci 27 (2001) 381–400.
[36] B. Christensen, Using X-ray computed tomography in hydrology: systems, resolutions, and limitations, J. Hydrol. 267 (2002) 285–297.